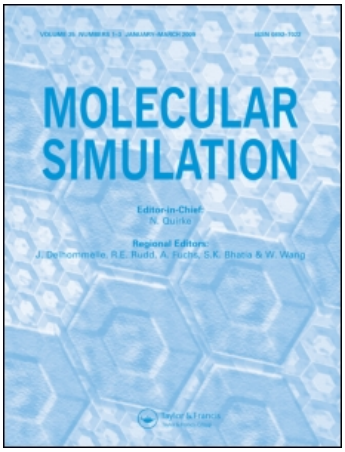

Molecular Simulation
Publication details, including instructions for authors and subscription information:
http://www.informaworld.com/smpp/title~content=t713644482

A dissipative particle dynamics model of carbon nanotubes

Orly Liba[a]; David Kauzlarić[b]; Zeév R. Abrams[a]; Yael Hanein[b]; Andreas Greiner[b]; Jan G. Korvink[b]
[a] Department of Physical Electronics, The Iby and Aladar Fleischman Faculty of Engineering, School of Electrical Engineering, Tel-Aviv University, Tel-Aviv, Israel [b] Laboratory for Microsystems Simulation, Department of Microsystems Engineering, The Albert Ludwig University of Freiburg, Freiburg, Germany

To cite this Article Liba, Orly , Kauzlarić, David , Abrams, Zeév R. , Hanein, Yael , Greiner, Andreas and Korvink, Jan G.(2008) 'A dissipative particle dynamics model of carbon nanotubes', Molecular Simulation, 34: 8, 737 — 748
To link to this Article: DOI: 10.1080/08927020802209909
URL: http://dx.doi.org/10.1080/08927020802209909

Molecular Simulation
Vol. 34, No. 8, July 2008, 737–748

Taylor & Francis
Taylor & Francis Group

A dissipative particle dynamics model of carbon nanotubes

Orly Liba[a], David Kauzlarić[b], Zeév R. Abrams[a], Yael Hanein[a]*, Andreas Greiner[b] and Jan G. Korvink[b]

[a]*Department of Physical Electronics, The Iby and Aladar Fleischman Faculty of Engineering, School of Electrical Engineering, Tel-Aviv University, Tel-Aviv, Israel;* [b]*Laboratory for Microsystems Simulation, Department of Microsystems Engineering, The Albert Ludwig University of Freiburg, Freiburg, Germany*

(*Received 11 March 2008; final version received 16 May 2008*)

A mesoscale dissipative particle dynamics model of single wall carbon nanotubes (CNTs) is designed and demonstrated. The coarse-grained model is produced by grouping together carbon atoms and by bonding the new lumped particles through pair and triplet forces. The mechanical properties of the simulated tube are determined by the bonding forces, which are derived by virtual experiments. Through the introduction of van der Waals interactions, tube–tube interactions were studied. Owing to the reduced number of particles, this model allows the simulation of relatively large systems. The applicability of the presented scheme to model CNT based mechanical devices is discussed.

Keywords: Carbon nanotubes; dissipative particle dynamics model; suspended tubes; vibrating tubes

1. Introduction

Carbon nanotubes (CNTs) are an exciting new material with a wide range of possible future applications. Of particular interest are mechanical nano structures consisting of individual nanotubes. These structures are marked by high material purity, very small mass and high resonance frequencies, and can thus be envisioned as building blocks for new devices such as high-frequency resonators or very small displacement sensors.

Simulations of the mechanics of CNTs are often performed in order to better understand or predict their behaviour. Simulation methods range from large-scale continuum-mechanics (CM) approaches, such as finite element (FE) analysis down to atomistic simulations, the most common being molecular dynamics (MD).

At the largest scale, mechanical simulation methods (e.g. FE) completely discard the atomic structure of the CNTs and rely only on their macroscopic elastic parameters [1]. To account for the discrete nature of the tubes and to facilitate simulations concerning the interactions between CNTs and other tubes or with their environment, atomistic methods such as MD are often used. In MD the atoms of the CNT are assigned with a potential such as the bond order potential developed by Terssof and Brenner (TB; [2]) or the molecular mechanics force field (MM3; [3]). As MD retains the atomic details of the molecule, it is able to simulate the interactions between CNTs with other materials (such as proteins and atoms) at the atomic level. MD also facilitates simulations concerning nano-scale effects, such as radial deformation caused by van der Waals (vdW) forces [4], CNT buckling [5], nanotube self-healing [6,7], nanotube growth, formation of *Y*-junctions, and tube–tube and tube–substrate interactions [8]. Another form of atomistic model is the structural mechanics approach [9]. In this model, the bonds between two nearest-neighbouring atoms act like load-bearing beams and each atom acts as the joint of the related beams. This method has been used to investigate the vibrations of nanotubes [10,11].

In atomistic methods, the number of particles in the simulation is equal to the number of atoms in the real systems, hence, as the scale of the system under consideration grows, the complexity of the simulated system becomes computationally challenging. Coarse-grained methods (e.g. dissipative particle dynamics (DPD); [12]) offer an attractive solution and allow computationally efficient mesoscale simulations. Using DPD, for example, it is possible to retain the particle-based structure of the system, while the number of particles in the simulation is reduced. An additional major advantage of DPD is the feasibility to seamlessly couple different length scales. Thus, simulations of multi-scale systems, such as CNTs on various substrates, interaction of CNTs with gas molecules, and the interaction of CNTs with one another can be easily and efficiently implemented. The dispersion of CNTs into a polymer matrix has already been modelled successfully using DPD and Flory–Huggins theory [13]. The CNTs in [13] were modelled as simple chains with a certain rigidity, while discarding the tubular structure of the CNTs.

Here, we present a mesoscale CNT model based on the DPD method which preserves the tubular structure of the CNT, so the mechanical properties of the tubes are reproduced. Our aim is to model realistic mechanical

*Corresponding author. Email: hanein@eng.tau.ac.il

ISSN 0892-7022 print/ISSN 1029-0435 online

DOI: 10.1080/08927020802209909
http://www.informaworld.com

behaviour of CNTs and their interactions with the environment. Our CNT DPD model is described below. We begin with a short description of the DPD simulation method. Next, a CNT model is constructed and its parameters are derived. In Section 4, we describe the calibration procedure and the derivation of the force constants, which account for the elastic properties of the CNT. A comparison between the DPD simulation and CM results is presented. In the next section, measurement of the Poisson's ratio and shear modulus of the DPD CNT are demonstrated and compared to experimentally measured values. Next, the tube–tube interactions are presented as an example of simulation of CNT interaction. Finally, the applicability of the presented DPD model to realistic CNT-based systems is discussed. Specifically, we consider the dynamics of tubes during the chemical vapour deposition (CVD) growth process and CNT based sensors.

2. DPD

In DPD [12], materials are represented by a set of point particles which stand for small portions of the material under consideration. Each DPD particle consists of N_{cg} MD particles, where N_{cg} may be called the coarse-graining number. The positions and momenta of the particles are updated in a continuous phase space at discrete time steps. The updates are computed by applying Newton's second law for a particle i of mass m_i

$$\dot{\mathbf{p}}_i = \mathbf{F}_i^{\mathrm{ext}} + \sum_{j \neq i} (\mathbf{F}_{ij}^{\mathrm{C}} + \mathbf{F}_{ij}^{\mathrm{D}} + \mathbf{F}_{ij}^{\mathrm{R}}), \tag{1}$$

$$\dot{\mathbf{r}}_i = \frac{\mathbf{p}_i}{m_i} = \mathbf{v}_i, \tag{2}$$

where $\mathbf{r}_i$, $\mathbf{p}_i$ and $\mathbf{v}_i$ are the position, momentum and velocity vector of particle i, respectively. $\mathbf{F}_i^{\mathrm{ext}}$ is a single particle force acting on particle i. The forces in the summation are pair forces between two particles i and j. $\mathbf{F}_{ij}^{\mathrm{C}}$ is a conservative force, $\mathbf{F}_{ij}^{\mathrm{D}}$ is a dissipative force, and $\mathbf{F}_{ij}^{\mathrm{R}}$ is a stochastic force. The specific form of the conservative forces used in our CNT model will be discussed in Section 3.2.

The dissipative and stochastic forces represent the energy lost to or gained from a heat bath. Therefore, for the isothermal DPD used in this work, $\mathbf{F}_{ij}^{\mathrm{D}}$ and $\mathbf{F}_{ij}^{\mathrm{R}}$ effectively represent a global thermostat. They set the correct temperature by fulfilling a fluctuation–dissipation theorem [14]. For our CNT model, we use an alternative approach for the implementation of the thermostat, which was introduced by Peters [15]. The reason for this choice is the superior stability properties of the Peters thermostat. This approach can also be extended to energy conserving, non-isothermal DPD [16].

The Peters thermostat partially relaxes the system under consideration to the equilibrium situation, which is assumed to be known *a priori* from statistical mechanics. The update equations for a pair of particles i and j are

$$\mathbf{v}_i' = \mathbf{v}_i + [-a_{ij}(\mathbf{v}_{ij}\cdot\mathbf{e}_{ij}) + b_{ij}\zeta_{ij}]\mathbf{e}_{ij}/2, \tag{3}$$

$$\mathbf{v}_j' = \mathbf{v}_j - [-a_{ij}(\mathbf{v}_{ij}\cdot\mathbf{e}_{ij}) + b_{ij}\zeta_{ij}]\mathbf{e}_{ij}/2, \tag{4}$$

which conserves linear and angular momentum. ζ_{ij} is Gaussian white noise with variance $2k_{\mathrm{B}}T/m$, where T is the equilibrium temperature the system attains due to the coupling to a heat bath and k_{B} is the Boltzmann constant. The proper variance and therefore the proper equilibrium distribution for the velocities is only achieved, if $b_{ij} = \sqrt{2a_{ij} - a_{ij}^2}$, which is the manifestation of the fluctuation–dissipation theorem for the Peters thermostat. Besides the condition $0 \leq a_{ij} \leq 1$, there is no further restriction on a_{ij}. We adopt Peter's choice of $a_{ij} = 1 - \exp(-2\gamma w(r_{ij})\Delta t)$, where the dissipation constant γ is a parameter of the model and determines the relaxation time of the system. A large dissipation allows relaxation of the system at fewer simulation time steps. Therefore, we choose a value for $\gamma = 10^7$, so, on average $a_{ij} \rightarrow 1$ for all particles i. We are currently investigating the effect of the dissipation on additional aspects of the model, such as the vibration of the tube and the quality factor. $w(r_{ij})$ is a weighting function depending on the scalar distance $r_{ij} = |\mathbf{r}_i - \mathbf{r}_j|$. Here, we use the second order polynomial

$$w(r_{ij}) = \begin{cases} \left(1 - \frac{r_{ij}}{r_{\mathrm{c}}}\right)^2, & r_{ij} < r_{\mathrm{c}} \\ 0, & r_{ij} \geq r_{\mathrm{c}} \end{cases}. \tag{5}$$

This weighting function vanishes smoothly at the cut-off radius r_{c}, which is set to 0.814 nm in this work. The cut-off radius of the thermostat is chosen to be the equilibrium distance between two lumped particles (Table 2) plus the size of one lumped particle in order to produce a fluctuation–dissipation interaction between close and neighbouring particles. Finally, Δt is the time step, also used for the numerical integration of the equations of motion (1) and (2). This integration can be performed by the conventional Velocity-Verlet algorithm [17] without any additional modifications [18], which is another advantage of the Peters approach.

The DPD simulation parameters are summarised in Table 1. The units of the simulation are described in Section 3.3.

Table 1. The DPD parameters.

Parameter	Description	Value
Δt	Time step	0.001
γ_d	Dissipation	10^7

3. CNT model

3.1 Structural model of CNT

As mentioned above, in DPD a material is constructed by grouping several atoms into lumped particles. The coarse-graining number used here, i.e. the number of carbon atoms lumped together into one particle, is $N_{cg} = 24$. The new structure retains the periodicity and the tubular shape of the underlying atomic structure, as shown in Figure 1.

The DPD CNT model presented here is thus equivalent to an armchair (6,6) structure. According to [19,20], given the chiral vector (**n**,**m**), the radius R of a CNT can be determined by using the relationship

$$R\,(\text{nm}) = 0.0392\sqrt{\mathbf{n}^2 + \mathbf{m}^2 + \mathbf{nm}}. \qquad (6)$$

This relation yields a tube radius of 0.407 nm. The DPD tube model is made of rings which consist of three lumped particles, as shown in Figure 1. Each ring is rotated around the axis of the tube by 60° relative to its neighbouring ring. The distance between particles in a single ring is defined by the triangle confined in the ring of radius R and is 0.705 nm. According to the model, the bond lengths between all of the neighbouring particles are equal, thus, the distance between rings is calculated and set to $h = 0.576$ nm.

Note that the model described here was designed for single wall CNTs (SWCNTs). For multiwall CNTs (MWCNTs) coarse-graining is possible, however, the interaction between the different walls has to be considered with care. We believe that the coarse-graining procedure for MWCNTS may involve anisotropic vdW interaction between the DPD particles. For simplicity, the vdW interactions used in this work to study tube–tube interactions (see Section 3.2) are assumed to be isotropic. This choice allows for qualitatively correct results as shown in Section 5.3.

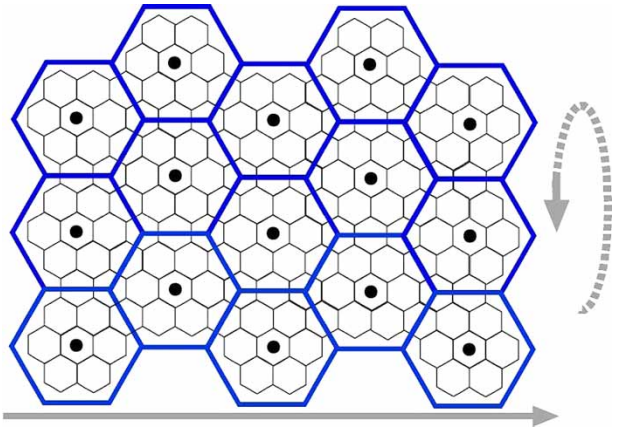

Figure 1. Schematic representation of the coarse-graining procedure of a CNT by grouping 24 carbon atoms. Solid dots represent the lumped particles. The solid arrow represents the axis of the tube. The dashed arrow represents the wrapping of the graphene to form a tube. This model is equivalent to an armchair nanotube with a chirality of (6,6).

Table 2. The parameters of the model.

Parameter	Description	Value
N_{cg}	Number of atoms in a lumped particle	24
n_p	Number of particles in each ring	3
R	Tube radius	0.5 mm
h	Distance between rings	0.576 nm
r_0	Equilibrium distance between particles	0.705 nm
α_r	Relative rotation angle of each ring	60°
n_r	Number of rings	Variable
L	Tube length	$n_r{\cdot}h$

To conclude this section, the parameters of the model are the coarse-graining number, N_{cg} and the number of particles in each ring, n_p. Resulting from N_{cg} are the equilibrium distance between lumped particles, r_0 and the distance between rings, h. The radius R, is determined by the number of particles in each ring, n_p. The relative rotation angle of two rings, α_{ring}, is set to 60°, according to the structure of the tube in Figure 1. These parameters can be changed in order to model a tube with a different diameter or coarse-graining number. The diameter of the tube can be scaled rather easily by increasing the number of particles in a ring. For example, tubes with 6 and 12 particles in a ring were simulated and proved to be stable. It has been shown, in experimental observations and MD simulations [21,20], that the elasticity of the nanotubes does not depend on their chirality. Thus, for the purpose of the model, which is to simulate mesoscale dynamics of CNTs, the model is sufficient even if it does not represent different chiralities of CNTs.

The characteristics of the tube structure simulated here are summarised in Table 2. The length of the tube is adjusted by setting the number of rings in the tube.

3.2 Particle forces

Since the particles in the DPD model are lumped particles, the forces contain empirical parameters, which are either derived analytically from reported properties of CNTs or calibrated by virtual tests. In this section we describe the forces acting between the lumped particles, which are the binding force, angular force and vdW interaction. These forces are depicted in Figure 2. The binding and angular force constants are set by calibration, which is described in Section 4. We use calibration in order to find the force

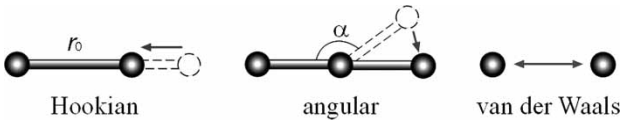

Figure 2. A schematic representation of the interactions between the particles of the DPD CNT model. The interactions between particles are Hookian, angular and vdW.

factors because the analytically estimated values did not reproduce the elastic properties of the CNT with enough accuracy. The vdW parameters are derived later in this section.

In the DPD CNT model presented here, the particles of the tube are bonded by forces acting between neighbouring particles. Each particle is connected to two neighbours on the same ring, two neighbours on the top ring and two on the bottom ring, forming six bonds for each particle (Figure 3).

To bond neighbouring lumped particles, we choose a Hookian spring force, $\mathbf{F}_{ij} = -k_{\mathrm{h}}(r_{ij} - r_0)\mathbf{e}_{ij}$, where $\mathbf{e}_{ij} = \mathbf{r}_{ij}/r_{ij}$ is the unit vector pointing from particle j to i and r_0 is the equilibrium distance between particles (Table 2). This form of spring force is used although it is infinitely extensible because the overall structure of the tube does not allow an infinite extension of the bonds, as shown later in the text. The force constant, k_{h}, is linked to the elastic properties of the tube. Its value is determined by the experimental tensile properties of the tube and is derived by calibration in Section 4.

To account for the stiffness of the tube, angular forces are added. The angular force is defined for three particles which form an angle, α, between them. The force is applied to triplets of neighbouring particles, which are aligned on the axis of the tube (Figure 4), rather than to nearest neighbours. This choice allows decoupling the spring force factor k_{h} from the bending force factor k_{a}. Decoupling these two forces enables us to calibrate k_{h} separately from k_{a} by performing virtual tests, in which the tube is not bent. In addition, applying the angular force only to triplets along the axis of the tube reduces the number of triplet interactions, which are computationally expensive. The angular potential is of the form $\mathbf{u}_a = -(k_{\mathrm{a}}/2)(\cos(\alpha) - \cos(\alpha_0))^2$ and the force is derived from $\mathbf{F} = -\nabla\mathbf{u}_a$. The exact form of the force on each particle can be found in [22]. The equilibrium angle of the force is $\alpha_0 = 180^\circ$ and the force constant, k_{a}, is determined by a calibration process, as will be described in Section 4.

In the simulations used for calibration only the steady state behaviour is of interest. Therefore, to dispose of the transient behaviour and reduce the simulation time needed for reaching the steady state, a numerical damping of the form $\mathbf{F} = -\eta\mathbf{v}$ is added, where η is the damping constant. η is assigned the value of 50, which gives a satisfactory reduction of the simulation time until steady state is reached. In these simulations, the numerical damping is used *instead* of the fluctuation–dissipation forces of the thermostat (Equations (1,3,4)), even though the dissipative force also produces damping, because steady state is reached more slowly. Another reason for omitting the fluctuation–dissipation forces from the calibration simulations is that they introduce thermal noise, which interferes with the measurements of the tube (the dissipation of Equation (1) cannot be used without the fluctuation because they are both combined in Peter's thermostat [15]).

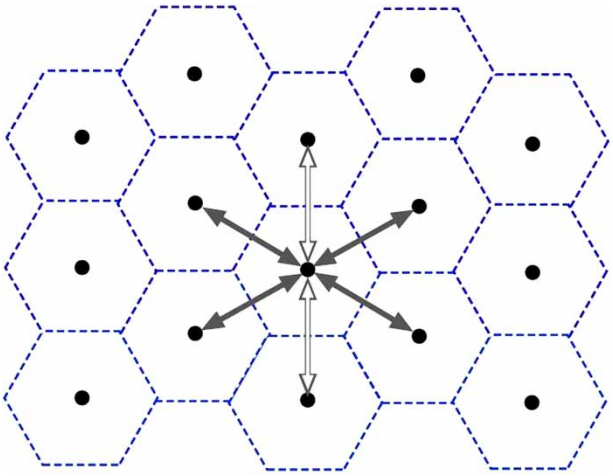

Figure 3. Schematic representation of the Hookian forces used in the DPD model. Solid dots represent the lumped particles. The arrows represent the Hookian bonds. The empty and full arrows represent bonds to particles in the same ring and to particles in different rings, respectively. The forces are attributed to every particle in the tube, each particle is connected to six neighbouring particles.

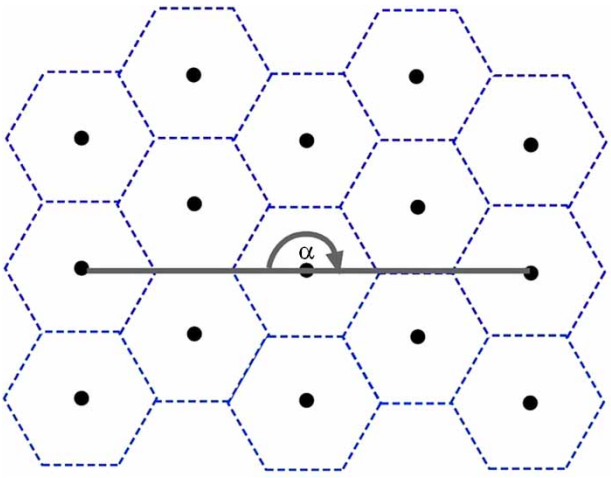

Figure 4. Schematic representation of the angular forces used in the DPD model. Solid dots represent the lumped particles. The arrow represents the angular force. The angular force is applied to every triplet of particles along the axis of the tube.

A vdW interaction is also added to the CNT model. This force is essential for the simulation of tube–tube and tube–surface interactions. For this interaction we choose the Lennard-Jones (LJ) potential

$$u_{\mathrm{LJ}} = 4\epsilon\left(-\left(\frac{\sigma}{r_{ij}}\right)^{6}+\left(\frac{\sigma}{r_{ij}}\right)^{12}\right), \tag{7}$$

which is applied on all the particle pairs in the simulation. The LJ potential has two parameters, the well depth ϵ of the potential, and the characteristic length σ, which is linked to the equilibrium distance between particles. For our model, the well depth is calculated based on the graphitic potential [23] by multiplying the LJ well depth of a carbon atom by N_{cg}. This calculation yields $\epsilon = 57.36\,\mathrm{meV}$. The equilibrium distance, $r_{\mathrm{LJ0}} = 2^{1/6}\sigma$ is chosen, so that the vdW force does not cause bond crossing [24]. According to [24], to prevent bond crossing the condition $r_{\mathrm{LJ0}} \geq r_0/\sqrt{2} = 0.498\,\mathrm{nm}$ should be satisfied, thus, r_{LJ0} is set to 5 nm and $\sigma = 0.445\,\mathrm{nm}$. The vdW cut-off radius is chosen to be $r_{\mathrm{vdW}} = 2.5\sigma$. This is a common choice and the effective range of the force, after which it becomes negligible. As was mentioned above (Section 3.1), in this study, an isotropic vdW force is used, but anisotropic vdW interaction between the DPD particles may be also considered.

The parameters of the forces of the DPD CNT model, k_{h}, k_{a}, η, ϵ, σ are summarised in Table 3.

3.3 Units of the simulation

All the calculations are made with the mass of the lumped particles and $k_{\mathrm{B}}T$ equal to one. Therefore, the units of mass and energy are

$$1m' = m_{\mathrm{p}}, \tag{8a}$$

$$1E' = k_{\mathrm{B}}T, \tag{8b}$$

where m_{p} is the mass of a DPD particle, which is equal to the mass of 24 carbon atoms. In order to minimise numerical errors all units are in the scope of the physical problem. The temperature regime is 300–1000 K and the length scale is in the nm range, therefore, the temperature unit, T' is set to 1000 K and the length unit, l' is 1 nm. All other units are then defined by the following four main units: mass, energy, temperature and length, as presented in Equations (9a)–(9f).

$$m' = 24{\cdot}12\mathrm{amu} = 478{\cdot}10^{-27}\,\mathrm{kg}, \tag{9a}$$

$$k_{\mathrm{B}}T = 1E' \Rightarrow E' = 1.38{\cdot}10^{-20}\,\mathrm{J}, \tag{9b}$$

$$T' = 1000\,\mathrm{K}, \tag{9c}$$

$$l' = 1\,\mathrm{nm}, \tag{9d}$$

$$t' = \sqrt{\frac{m'l'2}{E'}} = 5.885{\cdot}10^{-12} \cong 6\,\mathrm{ps}, \tag{9e}$$

$$F' = \frac{m'l'}{t'2} = \frac{E'}{l'} = 1.38{\cdot}10^{-11}\,\mathrm{N}. \tag{9f}$$

4. Calibration of the CNT model

In this section, we present the elastic behaviour of the CNT model and the calibration of the force constants by virtual experiments. In order to examine the elastic properties of the tube, it was subject to virtual tests of stretching and bending. Such simulations of experiments are commonly used in dynamic simulations (like MD) and allow manipulation of the tube in ways that are difficult or impossible to physically realise, e.g. clamping, bending, stretching or twisting the tube [26,27]. Measuring the reaction of the tube in these conditions enables us to determine the elastic properties of the DPD CNT. It is worth mentioning that different force fields, such as TB, MM3 and the DPD model, are expected to produce elastic properties that are very close to each other.

The virtual tests performed in the calibration of the model have shown that at small deformations the tube obeys CM relations. Therefore, we are able to calibrate the force constants, k_{h} and k_{a}, to obtain realistic elastic behaviour. Our results are consistent with previous reports, in which SWCNTs have been considered as continuum mechanical objects [21,25,26]. The elastic modulus and wall width to which we have fitted the model are 1 TPa and 0.335 nm (the graphitic layer spacing; [25]).

In the following sections, we find the elastic force constants, k_{h} and k_{a}, which reproduce the elastic properties of CNT as mentioned above.

Table 3. The force parameters of the model and their determination method.

Parameter	Description	Determination method	Value
k_{h}	Hookian spring force constant	Elongation strain versus axial stress	23,000
k_{a}	Angular force constant	Bending deflection versus pulling force	300
ϵ	Well depth of the vdW force	Calculated based on [23]	57.36 meV
σ	Characteristic length of the vdW force	Based on [24]	0.445 nm
η	Friction force constant	Arbitarary	50

4.1 Elongation

The Hookian force constant, k_h, can be found independently by merely elongating the tube. Based on CM, the elongation in the direction of the force is given by

$$\frac{\Delta L}{L} = \frac{F}{AE}, \tag{10}$$

where F is the applied force, ΔL is the elongation at the steady state, L is the unloaded length, $A = \pi(b^2 - a^2)$ is the cross sectional area of the tube, $a = r - w/2$ and $b = r + w/2$ are its inner and outer radii, w is the wall width of the tube and E is the Young modulus of the tube.

In this virtual test, we measure the elongation of a tube which is stretched by applying a constant force on one end and keeping the other end static (Figure 5). One could argue that by a simple spring model k_h could be derived directly from calculating the force for a small elongation. However, for the given coordinates of the particles, this results in a 20% lower value for k_h compared to the virtual test. This mismatch is due to the fact that the analytical calculation of k_h does not consider the radial compression of the tube and the vdW potential. The applied force acts on the three particles of the last ring, thus, the total force is the input force multiplied by three.

For this simulation, we remove the thermostat to eliminate noise and add numerical damping (of the previously mentioned form, $\mathbf{F} = -\eta\mathbf{v}$) in order to reach the steady state with fewer time steps. Adding or removing these interactions does not change the elastic behaviour of the tube because the contribution of the thermostat to the elastic properties is zero on average and because friction does not affect the steady state of the system.

The elongation in our virtual test is defined as the difference between the initial length of the tube, before the force is applied and its length at the loaded state. Once the force is applied, the tube starts oscillating (Figure 6). The loaded length of the tube is measured after these vibrations have been dissipated. Note that for this measurement it is important to make sure that the initial length is also the equilibrium unloaded length. This is done by simulating a tube without any external forces and making sure its length does not change. Figure 6 shows the length of the simulated tube as it changes with time until it reaches an equilibrium. As the tube elongates its cross-section is compressed. This behaviour is related to the Poisson's ratio of the tube, which is measured below, in Section 5.1.

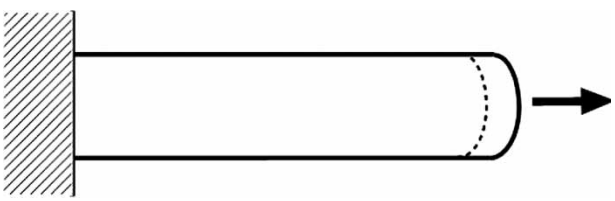

Figure 5. An illustration of a tube under elongation test. The tube is pulled from one end and fixed on its other end. This virtual test is used to calibrate the Hookian force in the DPD model.

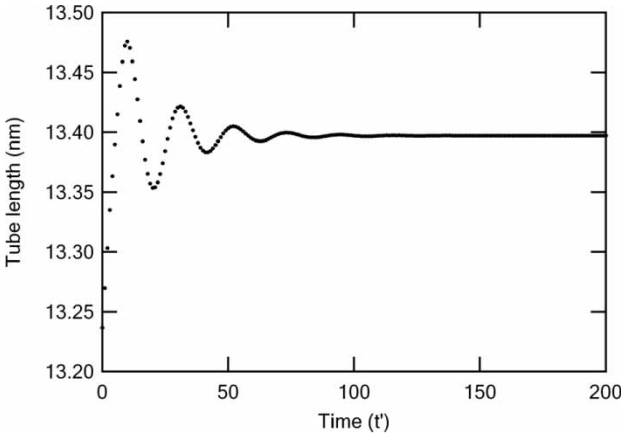

Figure 6. Tube length plotted versus time, from the initiation of the pulling force until it reaches the new equilibrium. The tube consists of 25 rings (corresponding to 14.4 nm) and is pulled by a force of $250\,F'$. The measured elongation is 0.16 nm.

To derive k_h, it was modified until the simulation results and Equation (16) yielded the desired Young modulus of 1 TPa. The Hookian force constant found in this way is $k_h = 23{,}000 \pm 400$ in the units of the simulation. The range of this value originates from the inaccuracy in measuring ΔL. To show that the CNT model behaves according to CM, similar simulations were done with different forces and with tubes of different lengths with $k_h = 23{,}000$.

Figures 7 and 8 show the dependence of the elongation and the strain on the length of the tube and on the applied

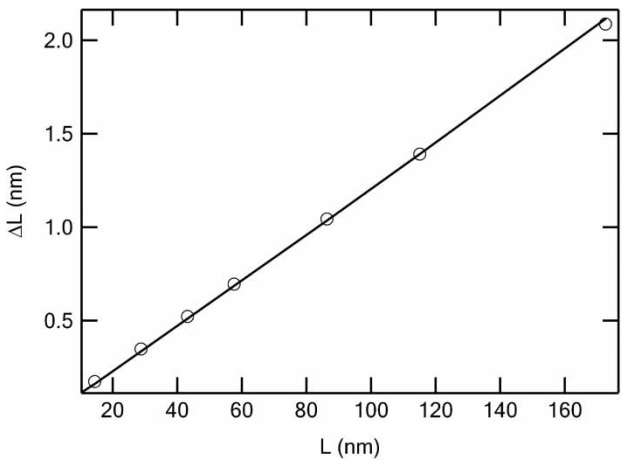

Figure 7. The steady state elongation of the simulated tube (open circles) plotted versus the initial length of the tube. The solid line represents the calculated curve from Equation (10). The applied force is $250\,F'$.

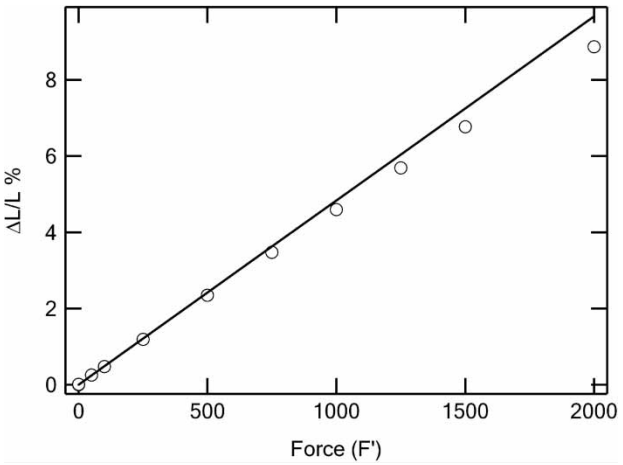

Figure 8. The elongation of the simulated tube (open circles) plotted versus the applied force. The solid line represents the calculated curve from Equation (10).The tube consists of 100 rings (corresponding to 57.5 nm).

force, respectively. These figures show a good fit between the simulation results and the theoretical expression of Equation (16).

In Figure 8, a deviation from a linear line is observed for large forces. This deviation is expected because at large deformations the assumptions of CM become invalid and saturation is expected, i.e. the tube cannot be elongated infinitely. The onset of the saturation is observed at a strain of approximately 3%. Note that this saturation would not occur if the tube was modelled as a 1D chain of particles connected by the same Hookian springs. The source of this saturation stems from the resistance of the cross-section of the tube to compression. This effect can be visualised from the drawing in Figure 3: The forces connecting the particles are not aligned along the axis of the tube, rather, they are at an angle of 30° (full arrows in Figure 3) or at an angle of 90° with the axis of the tube (empty arrows in Figure 3). In this configuration the cross-section of the tube is reduced when the tube is elongated. Thus, the forces connecting the particles along the cross-section of the tube (empty arrows in Figure 3) cause a resistance to the compression of the cross-section. This resistance results with a saturation of the elongation of the tube. Thus, compared to a 1D model, the presented 3D CNT model shows a saturation of the elongation even though the individual bonds between neighbouring particles do not saturate. The contraction strain and the elongation strain are discussed in Section 5.1, which describes the measurement of Poisson's ratio of the tube.

4.2 Bending deflection

So far, we have found the Hookian force constant, k_h, by simulating the elongation of the tube and by matching the results to the stress–strain relation of Equation (16). In this section, we find the second elastic force constant, k_a, which is the angular force constant described in Section 3.2. This will be done by bending the tube and measuring the force–deflection relation.

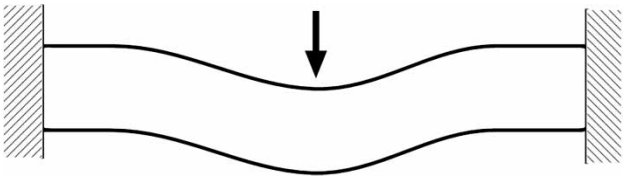

Figure 9. An illustration of a double clamped tube which is deflected by a force acting at its centre. This virtual test is used to calibrate the angular force of the DPD model.

In this simulation, we measure the deflection of the centre of a tube which is clamped at both ends and pulled at its centre by a constant force, as illustrated in Figure 9. The force acts on the central ring and as before, it acts on three particles, so the total force is the input force multiplied by three. As in the elongation simulations of the previous section, we remove the thermostat to eliminate noise and we add damping. The Hookian force constant, k_h, is included in the simulation and has the value that was found in the previous section.

Based on the Euler–Bernoulli theory which ignores the shear contribution (considered later in Section 5.2), the maximal deflection of a tube which is clamped at both ends is:

$$d = \frac{FL^3}{192EI}, \tag{11}$$

where d is the deflection, F is the applied force, $I = (\pi/4)(b^4 - a^4)$ is the second moment of inertia of

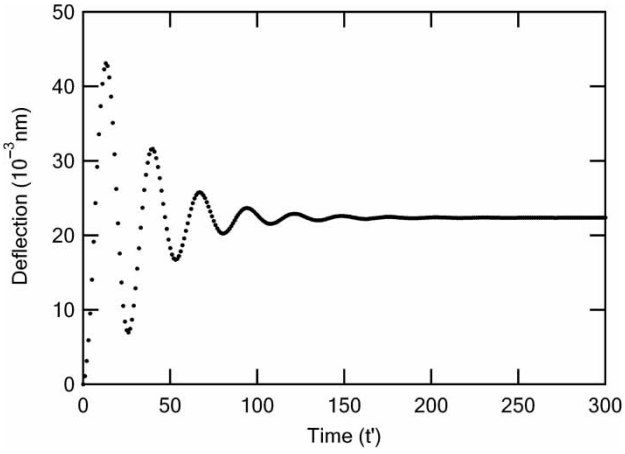

Figure 10. The deflection of the centre of the simulated tube plotted versus time from the initiation of the pulling force until the system reaches equilibrium. The tube consists of 100 rings, the measured deflection is 0.025 nm.

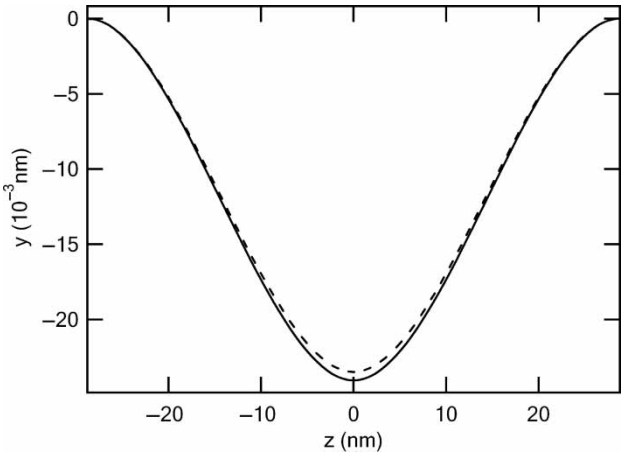

Figure 11. The deflection along the axis of the tube in steady state (dashed line) along with the theoretical deflection from Equation (18) (solid line). The tube consists of 100 rings and the applied force is $0.05\,F'$. The vertical and horizontal axes are in different scales to visualise the deformation of the tube.

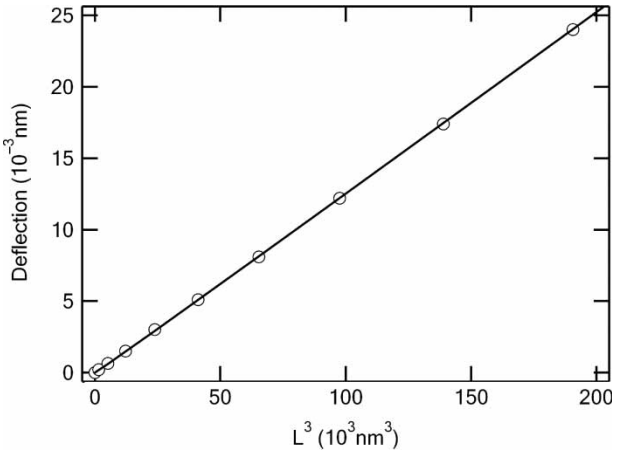

Figure 12. The deflection of the simulated tube at its centre (open circles) plotted versus the third power of the length of the tube. The solid line represents the calculated curve from Equation (11). The applied force is $0.05\,F'$.

the tube, a and b are the inner and outer radii of the tube, respectively.

The deflection is measured as the difference between the initial position of the centre of the tube and its final position after vibrations have been dissipated. Here as well, it is important to make sure that the initial length is also the equilibrium length. If the equilibrium length is different than the clamping distance, the tube is stretched or compressed and additional tension is created, which changes the deflection of the tube.

Figure 10 shows the deflection of the centre of the tube over time until it reaches its equilibrium value.

The force constant that was found by fitting the simulation data to the calculated deflection is $k_a = 300 \pm 10$ in the units of the simulation.

Once k_h and k_a are derived, all the force constants of the CNT model are known. They are summarised in Table 3.

To check that the bending of the CNT model behaves according to CM, the steady state profile of the bent tube is examined (Figure 11). The deflection along the axis of a double clamped beam subject to a force at its centre is derived from the Euler–Bernoulli equation and is described by

$$y = \frac{Fz^2}{48EI}(4z - 3L), \tag{12}$$

where y is the position of a length element of the beam along the direction of the force and z is the position of the element along the axis of the beam. In our simulation, y is the average position of the three particles in each ring. Figure 11 shows a good fit (with an error of 2.6%) between the shape of the DPD simulated tube to the shape calculated by CM. The discrepancy between the DPD result and the calculation is due to the fact that the CM relation in Equation (18) is an approximation for small deformations. The behaviour of the tube in the nonlinear regime is also shown in Figure 13. Another origin for the small yet apparent difference maybe due to the fact, that the tube is not completely equilibrated at the time of the measurement.

After fixing the angular force constant, similar simulations were done with different force values and tubes of different lengths. Figures 12 and 13 show that the dependence of the deflection on the length of the tube and on the applied force fit the theoretical expression of Equation (11) at small deformations. Note that in order to gain a better fitting, the length of the tube which is used for

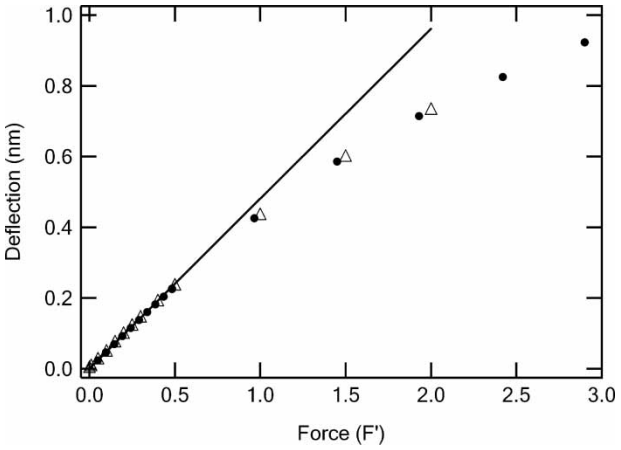

Figure 13. The deflection of the tube plotted versus the applied force. Empty triangles represent the DPD simulation results. Solid circles represent the ANSYS results. The solid line represents the calculated curve from Equation (11). The tube consists of 100 rings.

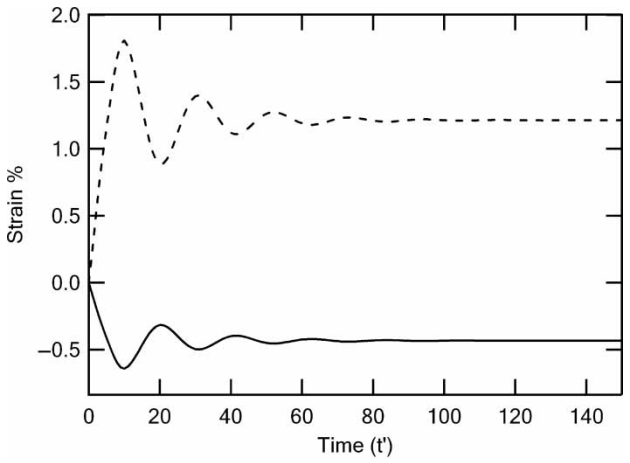

Figure 14. The lateral (solid line) and axial (dashed line) strains plotted versus time for a tube which consists of 25 rings and applied with an axial force of $250\,F'$.

the calculation of Equation (11), is measured with one ring less than n_r. This is justified because the rings on the edges of the tube do not fully participate in its deformation. By not including half of a ring from each end of the tube we obtain $L = h{\cdot}(n_r - 1)$.

At large deflections, we observe a deviation of the simulation results from the calculations based on Equation (11) (Figure 13). This deviation occurs at deflections larger than 0.5%. The origin of this discrepancy is that at large deformations the assumptions of the Euler–Bernoulli equation, which is the basis for Equation (11), become invalid. Similar results are obtained from continuum mechanics simulations with ANSYS (Ansys Inc., Ansys theory reference, http://www.ansys.com; also in Figure 13). The ANSYS simulation is done for a double clamped tube of the same size, with a Young's modulus of 1 TPa and linearly elastic material properties. We use a Newton–Raphson iterative solver in order to compute a static solution for large deformations.

5. Results obtained by the DPD CNT model

So far, we have described the DPD CNT model and showed how its force parameters were derived. It is now possible to perform various simulations of CNTs with this model. First, the Poisson's ratio of the tube is measured. Next, we derive the shear modulus of the tube and justify neglecting the shear deflection in the virtual test used for calibrating the angular force. The measurement of the shear modulus is compared to results obtained experimentally [28] and demonstrates the ability of the model to predict mesoscale mechanical behaviour of CNTs. Last, a simulation of tube–tube interaction is presented and compared to experimental observations.

5.1 Poisson's ratio

Poisson's ratio is the ratio of the relative contraction strain, or lateral strain (normal to the applied load) ϵ_x, divided by the relative axial strain (in the direction of the applied load) ϵ_y.

$$\nu = -\frac{\epsilon_x}{\epsilon_y}. \tag{13}$$

When simulating the elongation of the tube, one can also measure its Poisson's ratio by calculating the ratio of the cross-section strain to the elongation strain. From Poisson's ratio, we can calculate the shear modulus of the tube (elaborated in Section 5.2).

The lateral strain is measured by projecting every two adjacent rings on the xy plane (the plane which is perpendicular to the axis of the tube). The projected rings form hexagons, which are the new effective local cross-sections of the tube. The sides of each hexagon are measured and added to give an assessment for the local circumference of the tube, C_i, in which i is the index of the hexagon along the axis of the tube. The average $\langle C(t)\rangle$ of the local circumferences along the tube length is calculated for each time step. The lateral strain is measured using

$$\langle C(t)\rangle = \frac{n_r}{2}\sum_{i=1}^{n_r/2} C_i(t), \tag{14}$$

$$\epsilon_x(t) = \frac{\langle C(t)\rangle - \langle C(0)\rangle}{\langle C(0)\rangle}. \tag{15}$$

In Figure 14, the elongation and lateral strain are shown as a function of time for a tube with 25 rings and an applied axial force of $250\,F'$. The force is applied on one end of the tube, as illustrated in Figure 5. Figure 14 shows the expected behaviour of tube elongation along with lateral contraction. After the system stabilises the two strains are measured and Poisson's ratio is calculated.

Using this method Poisson's ratio was calculated for tubes of various lengths (10–150 nm) and found to be $\nu = 0.36 \pm 0.01$. To the best of our knowledge, this value has not been measured directly on CNT, however, it has been derived from several MD simulations. From Ref. [26] it is found to be 0.2 and 0.3 for the MM3 and Tersoff–Brenner potentials respectively, which is slightly lower than the result obtained here.

5.2 Shear modulus

From the Poisson's ratio the shear modulus G can be calculated as well. For an isotropic material the relation between shear modulus G and Young's modulus E is

$$G = \frac{E}{2(1+\nu)}. \tag{16}$$

When including the shear deformation, the deflection is (from Timoshenko's theory [29,30]):

$$d = \frac{FL^3}{192EI} + \frac{f_s FL}{4GA}, \tag{17}$$

where d is the deflection, F is the applied force, I is the second moment of inertia of the tube $I = \int y^2 \mathrm{d}A = (\pi/4)(b^4 - a^4)$, a and b are the inner and outer radii of the tube, respectively, and E is the Young's modulus of the tube $E(\mathrm{cnt}) \cong 1\,\mathrm{TPa}$. G is the shear modulus and f the shape shear factor (which is 10/9 for a cylinder). The shear effect is more noticeable for short tubes.

From Poisson's ratio which was found in the previous section and Equation (17), the calculated shear modulus, G, is $0.367 \pm 0.02\,\mathrm{TPa}$. Using Equation (17), we derive that the additional deflection due to shear is 1% of the total deflection for a tube of length 40 nm. For shorter tubes the shear deflection is more dominant and is 10% for a tube of length 14 nm. Thus, in the simulations used for calibrating the force factors k_h and k_a (in which, we used a tube of length 57 nm), the shear deflection is negligible.

Experimental measurement of the shear modulus of SWCNTs appears in [28] and a value of $G = 0.41 \pm 0.36\,\mathrm{TPa}$ is reported. The experimentally measured value is in proximity to the value, we obtained here by simulation. This demonstrates the predictive ability of the model to produce mechanical properties of the CNT, which are beyond the calibration process. In [26,31], the shear modulus is predicted by using the force constant model and an MD simulation, respectively. A value of $G = 0.455 \pm 0.02\,\mathrm{TPa}$ is reported in [31] and in [26] the obtained modulus is about one third of the Young's modulus and is also in agreement with our simulation.

5.3 *Tube–tube interaction*

To demonstrate the effectiveness of our model in studying CNT mechanics, we apply our model to one of the most fundamental aspects of CNT technology: the dynamics of CNTs during CVD growth. CVD is a common method to produce CNTs. In the CVD chamber, hydrocarbon gas (e.g. methane or ethylene) is heated to 900°C and undergoes pyrolysis. The carbon atoms attach to nanometer sized catalyst particles deposited on the substrate and grow in a nanotube form. As the tubes grow they widely vibrate until they bind to the surface. Tubes produced in this manner also exemplify strong adhesion to one another (Figure 15(a)). This effect is best manifested when tubes are grown from silicon pillar tops or over holes. In which case, extremely taut CNT networks are formed [32,33] due to a hypothesised zipper-like effect which is responsible for the tautness of the CNT structures [32].

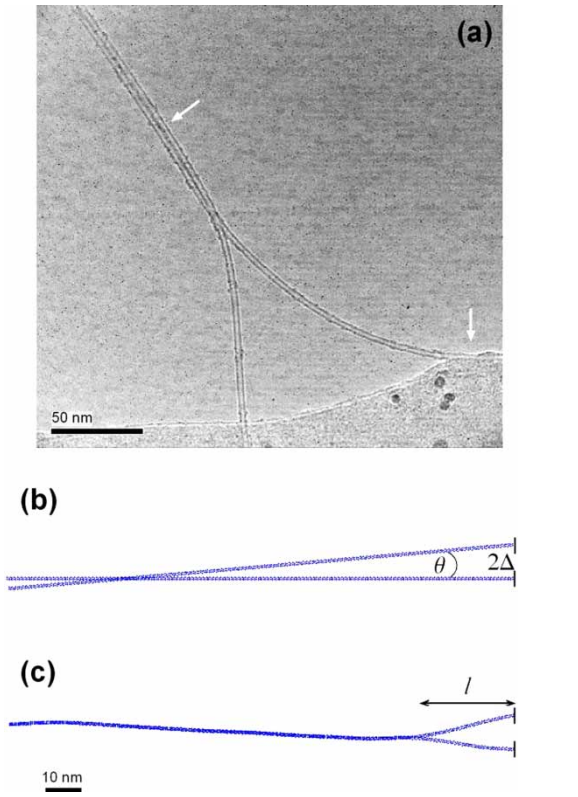

Figure 15. (a) Transmission electron microscope image of two adhering CNTs over a hole in a nitride grid after CVD growth. The arrows mark the places where tube–tube and tube–surface interactions are apparent. (b) The initial position of the tubes in the simulation. (c) The simulated tubes are at 0 K and at $t = 30\,\mu\mathrm{s}$.

In order to investigate this zipper effect with our DPD model, two tubes were realised as shown in Figure 15(b). The tubes are anchored at one end and positioned in such a way to form an initial angle of $\theta = 5°$. The distance between their fixed ends is 11 nm and the distance at the crossing point is 5 nm. The simulated temperature is 900°C, similar to the temperature in the CVD chamber. The tubes vibrate as a result of the thermostat and are brought closer inside the range of the vdW force. In this region, the tubes attract each other and bind. Note that external friction has not been added to this simulation and unlike the real CVD process in the model the tubes are in vacuum. DPD particles representing the surrounding gas can be added and are the subject of current investigations. We expect no significant influence of the absence of the surrounding atmosphere on the qualitative results for the zipping effect presented here. After some time of random vibrations the tubes enter the attraction region of one another and bind to each other. They attract until the vdW force is balanced by the internal elastic forces which prevent the tubes from further bending. After binding, the tubes continue to fluctuate together. The result of this

simulation is an example of the ability of the model to produce experimental observations, such as the binding of CNTs in the CVD process.

From the zipping process described above, the binding energy of the tubes can be calculated following the scheme presented in [34]. In [34] the binding energy of CNTs has been derived experimentally and fitted well with the theoretical derivation [23]. According to continuum mechanics theory the binding energy, γ_b, of two CNTs is [34]

$$\gamma_b = \frac{4EI}{l^2}\left(\theta - 3\frac{\Delta}{l}\right)^2, \tag{18}$$

where 2θ is the rotation angle between the tubes, 2Δ is the distance between their fixed ends and l is the distance from the fixed ends of the tube to the binding region, as demonstrated in Figure 15. Note that the thermal energy is not considered in this derivation, thus, the simulation for deriving the binding energy is performed at 0 K (the thermostat is deactivated). This enables a more accurate derivation of the binding energy. Because there are no thermal fluctuations, the tubes are initially brought within the attraction distance of the vdW force (the distance between the centres of the tubes is 1 nm). Otherwise, the initial conditions are similar to those of the simulation at 900°C described above. The final binding is shown in Figure 15(c). In our simulation, the measured distance l is 27 ± 1 nm, from which we obtain a binding energy of 0.093 ± 0.012 nN. The theoretical binding energy, which was calculated according to [23], is $\gamma_b = 0.1191$ nN.

5.4 CNT based devices

The tests presented above concerned with the fundamental mechanical properties of individual tubes. However, the DPD model presented here can also facilitate simulations concerning CNT based systems such as CNT oscillators [35]. In these systems, the interaction between the tube and its environment is of paramount importance. Of particular interest is the origin of interaction between the vibrating tube and the surrounding gas and the support substrate. Effects related to defects, slackness or tautness are important. Such systems can be effectively treated with our model and are currently under investigation.

6. Summary

A DPD model for simulating CNT systems at the mesoscale has been presented. The force constants of the model have been determined by fitting the simulation results to known mechanical parameters of CNTs. We showed that the elastic behaviour at small deflections is similar to the expected CM. After fixing the force constants, Poisson's ratio and the shear modulus were measured. Finally, the ability of the DPD model to simulate interactions has been examined.

It is important to note that the angular force in the presented model involves only the second neighbour triplets rather than including interactions with farther particles. Our desire to simplify the model arises from the need to simulate large-scale systems. The results of the calibration procedure and the additional data presented here have shown that the two-parameter model is accurate enough for the purpose of simulating mesoscale dynamics. In comparison to MD, which is the most suitable method for simulating microscopic phenomena, the presented model of the DPD CNT requires 1/24 of the particles to be simulated. Moreover, in the DPD model, the forces involve less particles (only pairs and triplets) and the time step is larger, resulting in a simulation program which needs much less time to compute.

Finally, in this work, we have concentrated on the conservative interactions of the DPD CNT model, however, DPD is also advantageous in describing thermodynamic behaviour. A report of the thermodynamics of the DPD CNT model is in preparation. Future work will also aim at modelling CNT based devices, in particular CNT resonators.

Acknowledgements

The authors would like to acknowledge partial funding by the Deutsche Forschungsgemeinschaft (DFG) via the Sonderforschungsbereich (SFB) 499 and by the Israel Science Foundation (grant no 1138/04).

References

[1] G.M. Odegard, T. Gates, L.M. Nicholson, and K.E. Wise, *Equivalent-continuum modeling of nano-structured materials*, Composites Sci. Technol. 62 (2002), p. 1869.
[2] D.W. Brenner, *Empirical potential for hydrocarbons for use in simulating the chemical vapor deposition of diamond films*, Phys. Rev. B 42 (1990), p. 9458.
[3] N.L. Allinger, Y.H. Yuh, and J.H. Lii, *Molecular mechanics. The MM3 force field for hydrocarbons. 1*, J. Am. Chem. Soc. 111 (1989), p. 8551.
[4] T. Hertel, R.E. Walkup, and P. Avouris, *Deformation of carbon nanotubes by surface van der Waals forces*, Phys. Rev. B 58 (1998), p. 13870.
[5] S. Iijima, C. Brabec, A. Maiti, and J. Bernhok, *Structural flexibility of carbon nanotubes*, J. Chem. Phys. 104 (1996), p. 2089.
[6] F. Ding, K. Jiao, M. Wu, and B.I. Yakobson, *Pseudoclimb and dislocation dynamics in superplastic nanotubes*, Phys. Rev. Lett. 98 (2007), p. 075503.
[7] C.-L. Zhang and H.-S. Shen, *Self-healing in defective carbon nanotubes: a molecular dynamics study*, J. Phys. Condens. Matter 19 (2007), p. 386212.
[8] A.N. Kolmogorov, V.H. Crespi, M.H. Schleier-Smith, and J.C. Ellenbogen, *Nanotube-substrate interactions: Distinguishing carbon nanotubes by the Helical Angle*, Phys. Rev. Lett. 92 (2003), p. 085503.
[9] C. Li and T.W. Chou, *A structural mechanics approach for the analysis of carbon naotubes*, Int. J. Sol. Struct. 40 (2003), p. 2487.

[10] ———, *Single-walled carbon nanotubes as ultrahigh frequency nanomechnical resonators*, Phys. Rev. B 68 (2003), p. 073405.
[11] ———, *Vibrational behaviors of multiwalled-carbon-nanotube-based nanomechanical resonators*, Appl. Phys. Lett. 84 (2004), p. 121.
[12] P.J. Hoogerbrugge and J.M.V.A. Koelman, *Simulating microscopic hydrodynamic phenomena with dissipative particle dynamics*, Europhys. Lett. 19 (1992), p. 155.
[13] A. Maitti, J. Wescott, and P. Kung, *Nanotube-polymer composites: insights from Flory-Huggins theory and mesoscale simulations*, Mol. Simul. 31 (2005), p. 143.
[14] P. Español and P. Warren, *Statistical mechanics of dissipative particle dynamics*, Europhys. Lett. 30 (1995), p. 191.
[15] E.A.J. Peters, *Elimination of time step effects in DPD*, Europhys. Lett. 66 (2004), p. 311.
[16] L. Pastewka, D. Kauzlarić, A. Greiner, and J.G. Korvink, *Thermostat with a local heat-bath coupling for exact energy conservation in dissipative particle dynamics*, Phys. Rev. E 73 (2006), p. 037701.
[17] D. Frenkel and B. Smit, *Understanding Molecular Simulation*, Academic Press, London, 1996.
[18] R.D. Groot and P.B. Warren, *Dissiptive particle dynamics: Bridging the gap between atomistic and mesoscopic simulation*, J. Chem. Phys 107 (1997), p. 4423.
[19] J.W.G. Wilder, L.C. Venema, A.G. Rinzler, R.E. Smalley, and C. Dekker, *Electronic structure of atomically resolved carbon nanotubes*, Nature 391 (1998), pp. 59–62.
[20] J.P. Lu, *Elastic properties of carbon nanotubes and nanoropes*, Phys. Rev. Lett. 79 (1997), p. 1297.
[21] R.S. Ruoff, D. Qian, and W.K. Liu, *Mechanical properties of carbon nanotubes: theoretical predictions and experimental measurements*, C.R. Physique 4 (2003), p. 993.
[22] D.C. Rapaport, *The Art of Molecular Dynamics Simulation*, 2nd ed., Cambridge University Press, Cambridge, 2004.
[23] L.A. Girifalco, M. Hodak, and R.S. Lee, *Carbon nanotubes, buckballs, ropes, and a universal graphitic potential*, Phys. Rev. B 62 (2000), p. 13104.
[24] P. Nikunen, I. Vattulainen, and M. Karttunen, *Reptational dynamics in dissipative particle dynamics simulations of polymer melts*, Phys. Rev. E 75 (2007), p. 036713.
[25] A. Krishnan, E. Dujardin, T.W. Ebbesen, P.N. Yianilos, and M.M.J. Treacy, *Youngs modulus of single-walled nanotubes*, Phys. Rev. B 58 (1998), p. 14013.
[26] A. Sears and R.C. Batra, *Maroscopic properties of carbon nanotubes from molecular-mechanics simulations*, Phys. Rev. B 69 (2004), p. 235406.
[27] M. Dequesnes, S.V. Rotkin, and N.R. Aluru, *Parameterization of continuum theories for single wall carbon nanotube switches by molecular dynamics simulations*, J. Comp. Electron. 1 (2002), pp. 313–316.
[28] A.R. Hall, L. An, J. Liu, L. Vicci, M.R. Falvo, R. Superfine, and S. Washburn, *Experimental measurement of single-wall carbon nanotube torsional properties*, Phys. Rev. Lett. 96 (2006), p. 256102.
[29] J.M. Gere and S.P. Timoshenko, *Mechanics of Materials*, 4th ed., PWS Publishing Company, Boston, 1997.
[30] J.P. Salvetat, G.A. Briggs, J. Bonard, R.R. Basca, A.J. Kulik, T. Stöckli, N.A. Burnham, and L. Forró, *Elastic and Shear Moduli of Single-Walled Carbon Nanotube Ropes*, Phys. Rev. Lett. 82 (1999), p. 944.
[31] J.P. Lu, *Elastic properties of carbon nanotubes and nanoropes*, Phys. Rev. Lett. 79 (1997), p. 1297.
[32] Z.R. Abrams and Y. Hanein, *Tube-tube and tube-surface interactions in straight suspended carbon nanotube structures*, J. Phys. Chem. B 110 (2006), pp. 21419–21423.
[33] Z.R. Abrams, Z. Ioffe, A. Tsukernik, O. Cheshnovsky, and Y. Hanein, *A complete scheme for creating predefined networks of individual carbon nanotubes*, Nano Lett. 7 (2007), pp. 2666–2671.
[34] B. Chen, M. Gao, J.M. Zuo, J.M. Zuo, S. Qu, B. Liu, and Y. Huang, *Binding energy of parallel carbon nanotubes*, Appl. Phys. Lett. 83 (2003), p. 3570.
[35] V. Sazonova, Y. Yaish, H. Ustunel, D. Roundy, T.A. Arias, and P.L. McEuen, *A tunable carbon nanotube electromechanical oscillator*, Nature 431 (2004), p. 284.